Carbohydrate Polymers 268 (2021) 118206

Contents lists available at ScienceDirect

Carbohydrate Polymers

journal homepage: www.elsevier.com/locate/carbpol

Transparent oxygen barrier nanocellulose composite films with a sandwich structure

Lanxing Du [a,b,c], Haonan Yu [a], Bohan Zhang [a], Ruilin Tang [b], Yang Zhang [b], Chusheng Qi [b], Michael P. Wolcott [c], Zhiming Yu [b,*], Jinwu Wang [d,*]

[a] College of Forestry, Hebei Agriculture University, Baoding 071000, China
[b] College of Material Science and Technology, Beijing Forestry University, Beijing 100083, China
[c] Composite Materials and Engineering Center, Washington State University, Pullman, WA 99163, USA
[d] Forest Products Laboratory, U. S. Forest Service, Madison, WI 53726, USA

ARTICLE INFO

Keywords:
Cellulose composite film
Sandwich structure
Oxygen barrier
Mechanism

ABSTRACT

Transparent gas barrier materials have extensive applications in packaging, pharmaceutical preservation, and electronics. Herein, we designed transparent films with a symmetric sandwich structure using layer-by-layer assembly of biaxially oriented polypropylene (BOPP) and acrylic resin (AR) followed by a cellulose nanoparticle (CNP) layer. The BOPP as a substrate created a barrier to hinder the transmission of water molecules to the adhesive AR layer and gas barrier functional CNP layer. The aspect ratio of the CNPs was shown to affect the film microstructure, resulting in different values for the oxygen transmission rate (OTR). The well-organized CNP layer exhibited lower OTR when compared with the network layer. The thickness, density, and porosity of the CNP layer exhibited correlations with OTR. The water molecules were able to flow in through an additional pathway, thus increasing the water vapor transmission rate (WVTR). Moreover, these sandwiched cellulose composite films showed excellent light transmittance and tensile strength.

1. Introduction

Non-renewable and non-degradable petroleum-based materials like polyethylene (PE), polypropylene (PP), polyethylene terephthalate (PET), and polyvinyl chloride (PVC) have been widely used for flexible food packaging or electronic devices since the last century. With increasing attention in global resource shortage and sustainable development, the interest in expanding the utilization of bio-based and biodegradable materials has driven researchers to focus on using biopolymers, such as polyhydroxybutyrate (PHB), polylactic acid (PLA), and polysaccharides (starch, chitin, and cellulose) (Siracusa et al., 2008; Vasile, 2018; Wang et al., 2017). Based on their inferior performance to petroleum-based counterparts in traditional packaging materials and electronic devices, adding additives to the composites, coating a thin layer on their surface, or forming a multilayered structure to improve various properties are effective and important strategies. Reactive oxygen and water cause food spoilage and electrical cutting-out in electronic devices, thus lowering oxygen transmission rate (OTR) and water vapor transmission rate (WVTR) are key solutions for packaging materials (Dou et al., 2015).

Recent progress has shown that cellulose, especially the cellulose nanoparticles (CNPs), are able to serve as oxygen barrier materials (Table 1). CNPs have high crystallinity, high length to diameter aspect ratio, and a considerable amount of hydroxyl groups on the surface. These characteristics enable CNPs to form a dense microstructure, presenting high potential as a gas barrier. Coating a thin layer of TEMPO (2,2,6,6-tetramethylpiperidine-1-oxyl)-oxidized CNPs on films of PLA, PP, oriented polyamide (OPA), and oriented PP (OPP) have led to composite films with outstanding oxygen barrier properties and ultrahigh transparency (Fotie et al., 2020; Fukuzumi et al., 2009). Dispersing CNPs in polymers decreased the oxygen permeability (Fang et al., 2019; Jung et al., 2020). Reinforcing the cellulose matrix with high aspect ratio materials of TiO_2, attapulgite, boron nitride, or montmorillonite resulted in excellent gas barrier properties (Nguyen et al., 2018; Roilo et al., 2018; Wang et al., 2018; Wu et al., 2012). Bacterial cellulose/acrylic resin composites, prepared by impregnating

* Corresponding authors.
E-mail addresses: lxydlx@hebau.edu.cn (L. Du), m18231385798@163.com (H. Yu), zbh2424596267@163.com (B. Zhang), trl08408022@126.com (R. Tang), bjfuzhangyang@bjfu.edu.cn (Y. Zhang), qichusheng@bjfu.edu.cn (C. Qi), wolcott@wsu.edu (M.P. Wolcott), yuzhiming@bjfu.edu.cn (Z. Yu), jinwu.wang@usda.gov (J. Wang).

https://doi.org/10.1016/j.carbpol.2021.118206
Received 7 December 2020; Received in revised form 12 May 2021; Accepted 12 May 2021
Available online 21 May 2021
0144-8617/Published by Elsevier Ltd.

Table 1
Thickness and oxygen transmission rate (OTR) of CNP-coated polymer films and commercially available polymer films.

Materials	Thickness (μm)	OTR (cm^3/(m^2·day))	Test conditions	Reference
SCNF/FP/PET film	90–91	0.98	room temp., 0% RH	Kim et al., 2020
FP/SCNF/FP/PET film	90–92	0.15	room temp., 0% RH	Kim et al., 2020
BOPP/PU/CNCs/PU/BOPP	174–178	5.7–6.1	23 °C, 80%RH	Wang, Chen, Wang, Gardner, & Tajvidi, 2020
BOPP/PU/CNFs/PU/BOPP	196–199	10.5–24.3	23 °C, 80%RH	Wang et al., 2020
BOPP/PU/PU/BOPP	160	238.6	23 °C, 80%RH	Wang et al., 2020
(GNPs/CNCs)n-coated PE-coated cardboard (layer-by layer assembly, 4–11 bilayer)	57.6–149.9 ($GNPs/CNCs)_n$ layer	608–2077	23 °C, 50%RH	Chemin, Heux, Guérin, Crowther-Alwyn, & Jean, 2019
NC coated BOPP/LDPE film	77.13 ± 3.35	24.02	23 °C, 75%RH	Lu, Guo, Xu, & Wu, 2018
BOPP/LDPE film	73.8 ± 1.71	67.03	23 °C, 75%RH	Lu et al., 2018
Bio-HDPE/CNF/bio-LDPE film	78	0.6 ± 0.1	23 °C, 0% RH	Vartiainen et al., 2015
	78	8 ± 3	23 °C, 50%RH	Vartiainen et al., 2015
	78	490 ± 20	23 °C, 80%RH	Vartiainen et al., 2015
HDPE/LDPE film (multilayer)	76	2140 ± 40	23 °C, 0% RH	Vartiainen et al., 2015
High density polyethylene, HDPE	80–100	2300–3300	25 °C, 0% RH	Ghosh et al., 2020
Polyethylene, PE	25	1543.09 ± 43.88	23 °C, 0% RH	Norrrahim, Ariffin, Hassan, Ibrahim, & Nishida, 2013
Poly(3-hydroxybutyrate-*co*-3-hydroxyvalerate), PHBV	25	218.4 ± 2.08	23 °C, 0% RH	Norrrahim et al., 2013
Polylactic acid, PLA	40.3 ± 0.47	541 ± 8.20	23 °C, 55 ± 1%RH	Sonar et al., 2020
PLA-PBAT blend (modified)	127 ± 1.25	330 ± 1.63	23 °C, 55 ± 1%RH	Sonar et al., 2020
PET/PE	70.0 ± 1.26	80.9 ± 2.15	23 °C, 55 ± 1%RH	Sonar et al., 2020
Polyvinyl chloride, PVC	50	896.45	25 °C, 70%RH	Mangaraj, Goswami, & Panda, 2014
Poly(vinyl alcohol-co-ethylene), EVOH	44	65.1	23 °C, 65%RH	Miao et al., 2019

Note:SCNF: succinylated cellulose nanofibers. FP: a type of fluorinated acrylic polymer, (NOVEC™ 1700); PET: polyethylene terephthalate; BOPP: biaxially oriented polypropylene; PU: translucent polyurethane; CNCs: cellulose nanocrystals; GNPs: gibbsite nanoplatelets; NC: nanocellulose; CNFs: cellulose nanofibers; LDPE: low-density polyethylene; PBAT: polybutylene adipate terephthalate.

the bacterial cellulose thin film in acrylic resin, formed a layered in-plane network structure with excellent flexibility and transparency, offering a material for potential innovation in the electronics device industry (Nogi & Yano, 2008). Multilayered alkyd resin/carboxymethylated cellulose nanofibril (CNF) films, multilayered cellulose nanocrystal/polyvinyl alcohol films, and multilayered cationic CNF/anionic vermiculite clay films using layer-by-layer deposition also display efficient oxygen barrier properties (Aulin & Ström, 2013; Ogunsona & Mekonnen, 2020; Qin et al., 2018).

Based on the "tortuous theory", the cellulose acts as a physical barrier structure to hinder the movement of oxygen gas molecules. Oxygen molecules exhibit kinetic diameters on the same order of magnitude as the diameters of the partially disconnected pores in the cellulose network, which does not allow transport through the film (Fukuzumi et al., 2011). This tortuous pathway varies in free volume shape, size, and quantity, and determines the molecular diffusion and permeation features. The free volume is generated by surface incompatibility between two components or is limited to the structures, and it cannot be eliminated even with elaborate design (Ammala et al., 2008; Dou et al., 2015; Kim et al., 2017). Therefore, it is still a challenge to develop novel high gas barrier materials.

This work aims to develop a new method to fabricate multilayer films of CNP and acrylic resin (AR) to be applied in flexible packaging materials. Five layers are designed in our study, consisting of BOPP-AR-CNP-AR-BOPP. The acrylic resin layers act as the tie layer between the BOPP and CNP, facilitating CNP to be uniformly coated on the surface of BOPP. This sandwich structure is believed to be an effective way to preserve gas and water vapor barrier properties of the components. The resulting sandwiched films were measured to determine their microscopic structure, surface energy, light transmittance, tensile strength, OTR, and WVTR.

2. Materials and methods

2.1. Raw materials

Cellulose nanocrystals (CNCs, slurry, ~11.8% solids) were made by the Forest Products Laboratory (Madison, WI) and purchased from the University of Maine Product Development Center. TEMPO-oxidized cellulose nanoparticles (T-CNPs) were prepared and characterized in our previous work (Du et al., 2018). The T-CNPs included TEMPO-oxidized microcrystalline cellulose (T-MCC), TEMPO-oxidized cellulose nanofibers (T-CNFs), and TEMPO-oxidized CNC (T-CNCs). The CNCs and T-CNPs are collectively referred to as CNPs. The characteristics of the T-CNPs and CNC are listed in Table 2. Acrylic resin (AR, Joncryl 678) was provided by BASF Co., Germany. Joncryl 678 is a styrene-acrylic acid copolymer with a molecular weight of 8600, an acid number of 215, and a density of 1.16 g/cm^3 at 20 °C. The ammonia hydroxide (28%) was purchased from Sigma-Aldrich Inc., USA. The corona-treated biaxially oriented polypropylene (BOPP, LPT-type) with a thickness of 57 ± 0.2 μm and density of 0.91 g/cm^3 was provided by Treofan Co., Raunheim, Germany.

2.2. Preparation of acrylic resin

The acrylic resin powder (2.6 g) was suspended in a solution (7.4 g) of 28 wt% ammonia (0.63 g) and deionized water (6.77 g) with sonication at room temperature until dissolved. The dissolved acrylic resin was labeled as AR.

2.3. Preparation of sandwiched films

A K control coater (RK K101, UK) was used to prepare the films with a sandwich structure, as shown in Fig. 1a. Coating thicknesses were calibrated with different wire rods in advance. A BOPP film of 25 cm × 20 cm acted as the substrate, and a vacuum adsorbed it onto the coating table. A 6-μm thick AR coating, i.e. adhesive layer, was applied to the surface of the BOPP film by a wire rod moving at a coating speed of 1.0 m/min. To obtain the continuous core layer, the T-MCC T-CNF suspensions (2 wt%, 100 μm coating thickness) and T-CNC, CNC suspensions (5 wt%, 40 μm coating thickness) were applied with a coating

Table 2
Mean values and standard deviations (in parentheses) of the properties of CNPs (Du et al., 2020).

Sample	Particle size		Crystallinity/%	Carboxyl group content/mmol/g	The viscosity of the CNP suspension (2 wt%) at the shear rate of 10^3 s^{-1}/mPa·s
	Length/nm	Diameter/nm			
T-CNFs	174 (88)	3.6 (1.3)	62.5	2.78	15.818
T-MCCs	149 (83)	6.5 (5.4)	77.4	2.79	8.5737
T-CNCs	108 (60)	5.9 (3.0)	79.4	1.99	1.7087
CNCs	234 (119)	20 (9)	84.3	–	4.7105

speed of 0.6 m/min after the AR layer was totally dried. Finally, the subsequent AR coating was completed following the method above and then the other BOPP substrate was applied. These five-layered films were marked as BOPP-AR-x-AR-BOPP, where the x refer to T-CNF, T-MCC, T-CNC, or CNC. The sandwiched film without CNPs, i.e. the film of BOPP-AR-AR-BOPP, was fabricated for comparison. The sandwiched films were stored at 23 ± 2 °C for testing.

2.4. Characterization

2.4.1. Transmittance

Regular light transmittances were measured at wavelengths from 200 nm to 800 nm with a Lambda 25 UV/VIS Spectrometer (Perkin Elmer, USA). The spectrum of air was set as a reference for the sandwiched films. The light transmittance value was determined at a wavelength of 600 nm.

2.4.2. Surface roughness

Atomic force microscopy (AFM) (Bruker Multimode 8, USA) with triangular-shaped cantilevers (spring constant, 0.06 Nm^{-1}) was used to characterize surface morphology. The AFM image of the surface of each layer was obtained after the coating was dried. Surface roughness as reflected by arithmetic mean deviation of the profile (R_a) was calculated from AFM images with NanoScope Analysis software.

2.4.3. Morphology and structure

The cross-sectional images of the resulting films were observed by scanning electron microscopy (SEM) (FEI SEM Quanta 200F, USA) at a 5 kV accelerating voltage. The film surfaces were fixed in parallel fixed on carbon adhesive disks and the naturally fractured films were vertically fixed. They were sputter-coated with platinum at a thickness of 2.8 nm. The thickness of the adhesive layer and core layer could be reflected by the tearing section in the SEM images. The accurate thickness of each layer was calculated by ImageJ image analysis software.

2.4.4. Surface energy

The contact angle (θ) was measured using a Dynamic Surface Analysis system (VCA Optima, AST Products INC., USA) equipped with a video camera and software for image analysis. A drop of probe liquid (distilled water, formamide, diiodomethane) was deposited on the sample surface, and an image of the drop was obtained to measure the contact angle. The surface energy was calculated by the geometric mean Eq. (1) based on the static contact angle measurements with the probe liquids.

$$\gamma_{sl} = \gamma_s + \gamma_l - 2\left(\sqrt{\gamma_s^d \gamma_l^d} + \sqrt{\gamma_s^p \gamma_l^p}\right) \quad (1)$$

where γ refers to the surface energy, γ^d refers to the dispersive component and γ^p is the polar component, $\gamma = \gamma^d + \gamma^p$. The subscripts s and l designate liquid and solid respectively. γ_{sl} is the solid/liquid interfacial energy, γ_s is the solid surface energy, γ_l is the liquid surface energy. The relationship between γ_{sl}, γ_s and γ_l is described by Young's Eq. (2):

$$cos\theta = (\gamma_s - \gamma_{sl})\gamma_l \quad (2)$$

A combination of Eqs. (1) and (2) gives the following relationship:

$$(1 + cos\theta_l)\gamma_l = 2\left(\sqrt{\gamma_l^d \gamma_s^d} + \sqrt{\gamma_l^d \gamma_s^p}\right) \quad (3)$$

where the known surface free energy dispersive (γ^d) and polar (γ^p) components of the three probe liquids from literature and three measured contacted angles were substituted to give Eq. (3). The polar and dispersive components of the solid surface energy were approximated by solving three equations with the least-squares method.

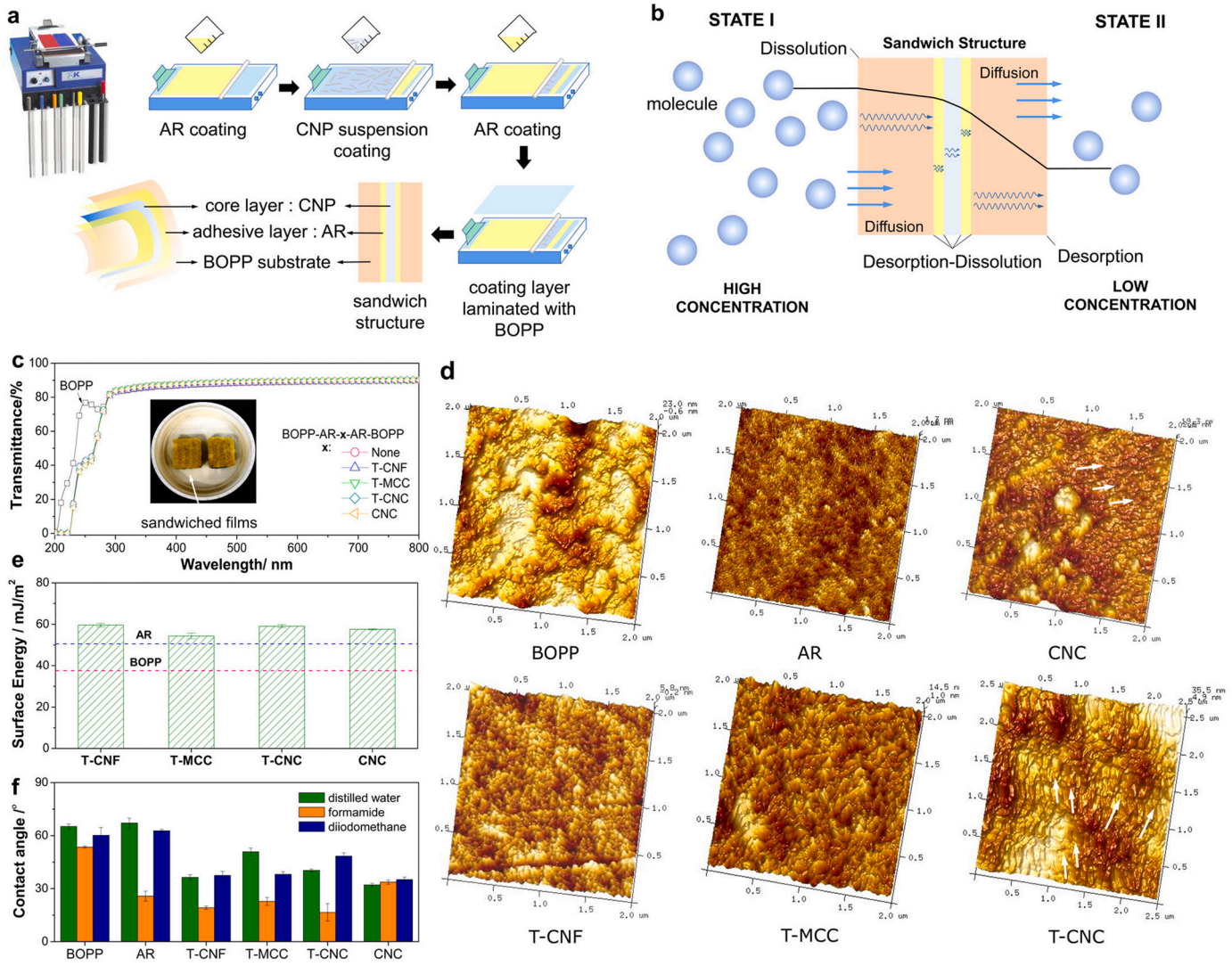

Fig. 1. (a) The laminating process and the film the symmetric sandwich structure; (b) the oxygen or vapor transmission mechanism across the sandwiched film; (c) the light transmittance of the sandwiched films in a wavelength range from 200 to 800 nm; (d) the three-dimensional morphologies of the surface of the BOPP, AR, and CNP layers; the surface energy (e) and the contact angles (f) of CNP layers.

2.4.5. Tensile strength and elongation at break

The tensile strength and elongation at break of BOPP and sandwiched films were measured using an Instron 4466 (Instron Co., USA) following the ASTM D882-12 standard with an initial grip separation of 50 mm and separation rate of 500 mm/min. The films were stored at 23 ± 3 °C and 50% RH for two weeks before testing.

2.4.6. Oxygen transmittance rate (OTR) and water vapor transmittance rate (WVTR)

The OTR of BOPP and sandwiched film samples (10 cm × 10 cm) were measured by Mocon OX-Tran 2/21 (Mocon Inc., USA) according to the ASTM D3985 standard with a condition of 23 °C and 0% RH. One side of the film was exposed to flowing nitrogen gas, and the other side was exposed to flowing oxygen gas. The amount of permeated oxygen for a specific period was measured by a detector when the transmission reached the steady-state. It took 12 to 16 h to complete one test. Water vapor transmittance rate was measured by Mocon Permatran-w3/33 (Mocon Inc., USA) equipped with an infrared sensor to detect water vapor transmittance, following ASTM F1249. The OTR and WVTR were calculated based on the following equations:

$$\mathrm{OTR} = (\mathrm{dV}/\mathrm{dt})/\mathrm{A} \quad (4)$$

$$\mathrm{WVTR} = (\mathrm{dm}/\mathrm{dt})/\mathrm{A} \quad (5)$$

where dV/dt or dm/dt is the volume or mass of permeated oxygen or water vapor across the area (A) per unit time.

2.4.7. Density and porosity

The thick AR layer caused cracking. Therefore, a thin AR layer was prepared by controlling the amount of AR application. The coating weight of AR layer and CNP layer were determined by weighting the film before and after coating (weighting the pure BOPP, AR-coated BOPP, CNP-coated AR/BOPP). The thickness of each layer was determined on the SEM images of the cross-section of the film with the ImageJ image analysis software. The density was calculated by dividing the weight by the calculated volume. Porosity was calculated by the following equation:

$$P = (\rho_0 - \rho) \times 100\%/\rho_0 \quad (6)$$

whereas P is porosity, ρ_0 is the cellulose density (assumed to be 1.55 g/cm^3), and ρ is the density of the CNP layer.

3. Results and discussion

3.1. Transmittance

The BOPP and sandwiched films appeared to be transparent with a transmittance at 600 nm in a range from 89.1% to 89.4%. Upon adding the CNP layer, the sandwiched structure barely influence the resultant light transmittance (Fig. 1c). Sun et al. (2015) reported that the T-CNP films showed transmittance values greater than 90% at 600 nm, and the transmittance at 900 nm for T-CNP films reached up to 98.4%. BOPP and CNPs are composed of well-organized crystals. When a beam of light hits the interface between two different materials, such as air to BOPP, or BOPP to CNPs, the light deviates from the original track due to scattering. The reflection and diffuse reflection block a portion of light at the film surface, leading to reduced transmittance, and the remaining light is refracted, allowing continued access to the crystals. Thus, the transmittance is related to the surface roughness at the interface between layers, the pathway length of light in crystals, the crystallinity of BOPP or CNPs, and the number of layers. The sandwiched films with several interfaces disrupting the light transmission still displayed high transmittance, indicating the films had a smooth interface, high crystallinity, and a small amount of scattering. This high transmittance is beneficial for packaging and electronics applications.

3.2. Surface roughness

Fig. 1d shows the micro-profiles of the film surfaces. The BOPP film was corona-treated by the supplier and was ravine-like with surface roughness, R_{aBOPP} of 5 nm. Generally, an uneven surface has more mechanical connecting sites and larger aspect ratio to provide anchor points for the coating, improving the adhesion between the coating and substrate. However, too high R_a could reduce the wettability of the surface and result in adhesion defects (Rowe, 1978). The AR layer covered on the corona-treated BOPP presents a smooth surface with R_{aAR} at 0.24 nm without significant concavity and convexity. It indicates the AR flowed well and was uniformly dispersed, and the surface roughness of the BOPP substrate was appropriate. The R_a of T-CNF, T-MCC, T-CNC, CNC layers were 2.83 nm, 2.81 nm, 4.95 nm, and 2.22 nm, respectively. The differences in aspect ratio and particle size of the CNPs accounted for slight differences in R_a and different surface morphologies. The T-CNFs formed a uniform and irregular particle distribution, resulting in a network structure. The T-CNCs and CNCs eventually became oriented structures, while the T-MCCs had a mixture of the network and oriented structure (Du et al., 2020). The $R_{aT\text{-}CNC}$ was much higher than others. It might be ascribed to the small particle size of T-CNC and the low viscosity of T-CNC suspension (Table 1). During the film formation, water gradually evaporated, and the concentration of T-CNC suspension increased. The extremely small T-CNC individuals with a relatively low aspect ratio easily moved and were organized by self-assembly locally. The assembled T-CNCs resulted in the inhomogeneous distribution in the aqueous phase. The local aggregation gradually generated an uneven surface with ongoing evaporation. Meanwhile, the low viscosity means less internal friction. Under the shear force generated by wire rod movement, the dispersed T-CNCs moved along the force direction without strong disruption, resulting in the formation of the overall uneven surface.

3.3. Surface energy

According to the geometric mean method, the surface energy of each layer was calculated based on contact angle analysis (Fig. 1e,f). The BOPP had a rather low surface energy (38.4 mJ/m^2), making it difficult to achieve surface wetting, inking, and gluing. It resulted from a well-organized structure, high crystallinity, abundant methyl groups on the BOPP surface, stretching orientation, and the ability to automatically decrease the energy to maintain stability. When the AR was coated on the BOPP as an adhesive layer, the surface energy reached up to 50.9 mJ/m^2. Although the surface roughness of the AR was lower than that of the BOPP, the AR had a low molecular weight, a considerable amount of carboxyl groups, and strong surface shrinkage generated by self-crosslinking, and these enhanced the surface energy and functionally improved the adhesion between BOPP and CNPs.

The surface energies of the T-CNF, T-MCC, T-CNC, and CNC layers were 59.6, 54.3, 59.1, and 57.5 mJ/m^2, respectively. They presented higher surface energy than BOPP and AR, due to a combined effect of the hydrophilic groups, aspect ratio, crystallinity of the cellulose, the porosity and surface roughness of the resultant films. The CNPs in this study had a large number of hydroxyl groups (-OH) and carboxyl groups (-COOH), showing a greater affinity for water molecules and forming hydrogen bonds. The T-CNFs had the largest aspect ratio and relatively low crystallinity, thus improving the wettability and surface energy. Compared with T-CNFs, the T-MCCs had equivalent carboxyl groups and surface roughness, but their higher crystallinity resulted in lower surface energy. The high roughness of the T-CNC layer led to a higher surface energy than the CNC layer.

3.4. Tensile strength and elongation at break

Adding the CNP layer significantly increased the tensile strength of the sandwiched films (Fig. 2a). The films with the T-CNF, T-MCC, T-CNC, and CNC layers showed tensile strengths of 203.7 MPa, 196.0 MPa, 190.8 MPa, and 160.5 MPa, respectively. Wakabayashi et al. (2020) reported that fibrillation contributes to the mechanical properties and the increased aspect ratio increases the contact area when forming the film between individual nanofibers. Therefore, the increased interweaving ability enhanced the tensile strength of the T-CNP thin layers, especially the T-CNF layer. Moreover, the tensile strength was affected by the degree of polymerization, surface oxidation, and adhesion between fibers, even the aldehyde groups on cellulose could increase the mechanical properties (Saito & Isogai, 2006). The elongation at break of the sandwiched film slightly reduced compared to the pure BOPP and the sandwiched film without CNP layer (Fig. 2b). It resulted from the considerable amount of hydrogen bonds between cellulose constraining slipping between molecules. However, the limited reduction barely influenced on its application in packaging.

3.5. OTR

The OTR of the sandwiched films are shown in Fig. 2c except for the BOPP, owing to its OTR exceeding the instrument testing range under 23 °C and 0% RH. It was found that the OTR considerably decreased by adding the CNP layer. The OTR of films with the T-CNF, T-MCC, T-CNC, and CNC layers were 11.83, 18.68, 2.36, and 5.59 cc/(100in^2·day), respectively. The particle size, porosity after film formation, and film density had a combined influence on the OTR (Fukuzumi et al., 2011; Fukuzumi et al., 2013). When the same amount of CNPs was sandwiched in the films, a different thickness was formed due to the different nanoparticle morphologies. The parallel arrangement or well-organization of cellulose nanoparticles generally resulted in a denser structure, impacting the OTR. This will be discussed in detail in the mechanism section.

3.6. WVTR

The films without a CNP layer had a WVTR of 0.1880 g/(100in^2·day). The sandwiched films with a CNP layer displayed high WVTR values, as shown in Fig. 2d. This is ascribed to the hydrophilicity of the CNPs. The chemical groups on the CNP surfaces were able to absorb and transport water molecules, accelerating water molecule movement in the films. The films had five layers, and each layer had different microstructures. As a result, water molecules exhibited a slow-quick-slow movement, leading to increased WVTR. Meanwhile, the OTR

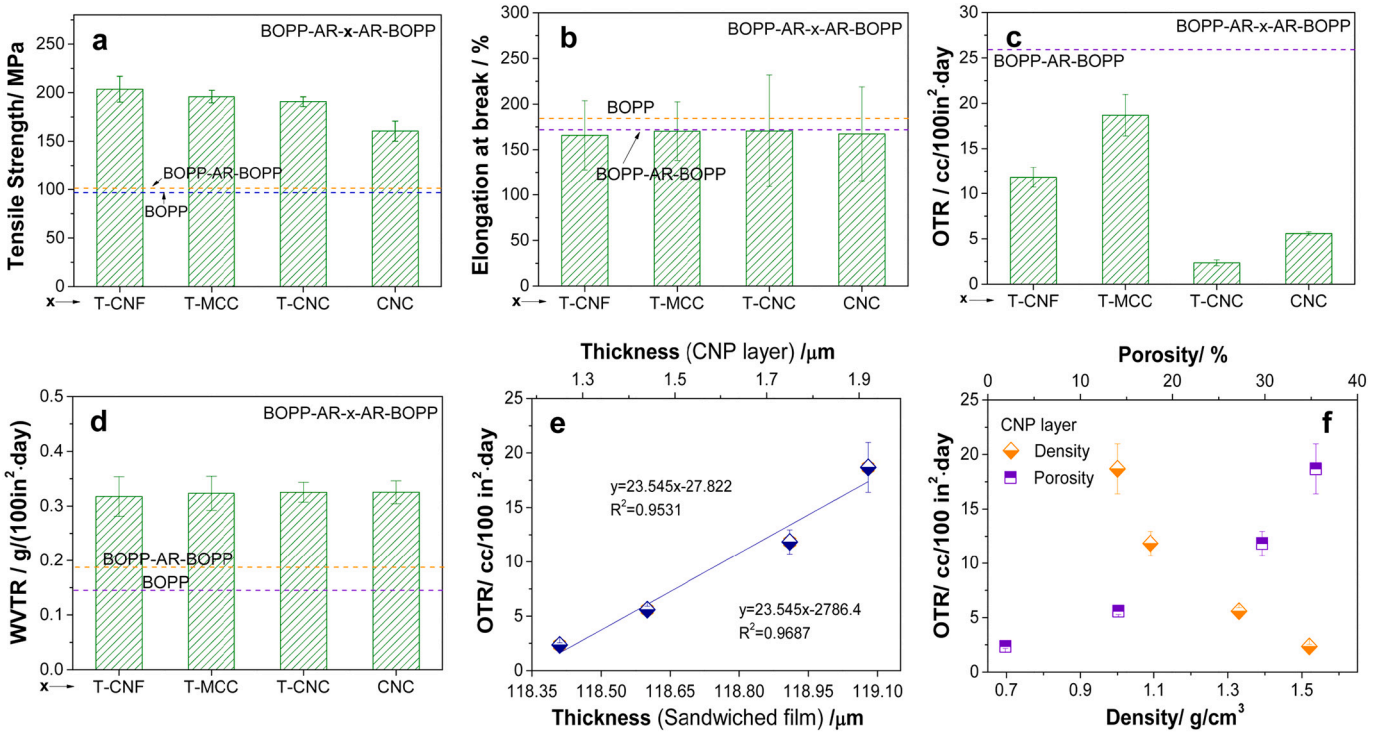

Fig. 2. The properties of the sandwiched films (a) tensile strength; (b) elongation at break; (c) OTR; (d) WVTR; (e) the correlation of OTR against thickness of the sandwiched films or CNP layers at the same coating weight; (f) the correlation of OTR against porosity and density of the CNP layer at the same coating weight; the x-axis was the thickness or density/porosity of the core layer of the 5-layered films.

of the CNP films decreased after water absorption (Vartiainen et al., 2015). The BOPP showed excellent WVTR, 0.1492 g/(100in^2·day). It was designed to be the surface layers of the sandwiched film, protecting the coral CNP layer from direct water absorption. This is an advantage of the sandwich film structure. However, from a CNP layer perspective, the WVTR of the sandwiched films were not significantly different with T-MCC, T-CNF, CNC, and T-CNC at 0.3174, 0.3232, 0.3251, and 0.3252 g/(100in^2·day), respectively. This indicated that the WVTR was largely decided by the BOPP layers, which masked the effect of the aspect ratio and carboxyl groups on the WVTR.

3.7. Barrier mechanism of the sandwiched films

The five-layered structure of the film is observed in Fig. 3a–f. The fractured AR cross-sections are rough and irregular. It is assumed that AR macromolecules might be assembled into thin lamellae that are naturally fractured along the weak molecular bonding strength between lamellae, creating this fracture texture. Different from the AR layer, the cross-section of the fractured CNP layer was smooth and dense. During the drying of the coated CNP suspension, individual nanoparticles adjusted their orientation cooperatively and drew closer with water evaporation and eventually formed hydrogen bonds. Moreover, the aspect ratio of CNPs influenced the microstructures of the cellulose layer, displaying a network or parallel structure or a combination of both. These different microstructures showed different tortuous pathways affecting the resultant gas barrier properties.

Gas or vapor molecules experience three processes in each layer before they can completely permeate through the film, i.e. dissolution, diffusion, and desorption as shown in Fig. 1b. According to Fick's law, the diffusion coefficient, dissolution coefficient, and other factors determine the molecular permeability of the sandwiched films. Intrinsically, permeation rates depend on the microstructure, density, porosity, and other properties of the films. CNPs have been investigated as the barrier matrix or barrier reinforcement in composites to change or extend the permeation pathway, resulting in increased barrier properties (Fukuzumi et al., 2009; Wang et al., 2018). It is generally believed that gas or vapor molecules bypass CNPs due to their high crystallinity. In this study, the laminating structure replaced the traditional mixture structure. The multilayer structure increases the complexity of the permeation, subjecting the molecules to multiple dissolution, diffusions, and desorptions in different layers. As a continuous layer, CNPs prevent oxygen permeation by using their high crystallinity and self-assembling property (Fukuzumi et al., 2009). BOPP at the surface layer protect the core layer from being directly exposed to the water vapor.

Fig. 3g shows the schematic models of the microstructures of the CNP layers. Most of the T-CNFs were randomly oriented as a network structure in-plane, exhibiting large gaps between particles in plane. Compared to the T-CNFs, T-MCCs had a larger diameter and relatively lower aspect ratio, generating large steric hindrance and gaps between particles larger than those in the T-CNFs. The T-CNCs and CNCs had spindle-like shapes and were oriented in one direction via hydrogen bonding, reducing the distance between each other to less than the kinetic diameter of oxygen (0.346 nm) (Jasińska et al., 2003). On the other hand, the formed gaps generated versatile pores for molecular permeation. The pore sizes and porosity determine the molecular permeation channels and permeation rates. Thus, it can be said that CNP morphology affected the resulting film microstructure. These different microstructures account for the differences in oxygen and water vapor transmission rates.

For the sandwiched films, the OTR showed a positive linear relationship with film thickness (Fig. 2e). The thickness variation was due to the CNP layers for which the same coating weight was applied for different types of CNPs. When the water evaporated, different CNP types created different internal structures. When the CNP layer was thicker and it was also porous and lower in density. Based on these observation, it was found that the OTR showed a positive correlation with CNP thickness and a negative correlation with the density and porosity of the CNP layer (Table 3, Fig. 2e, f). Under the same coating weight, the CNP

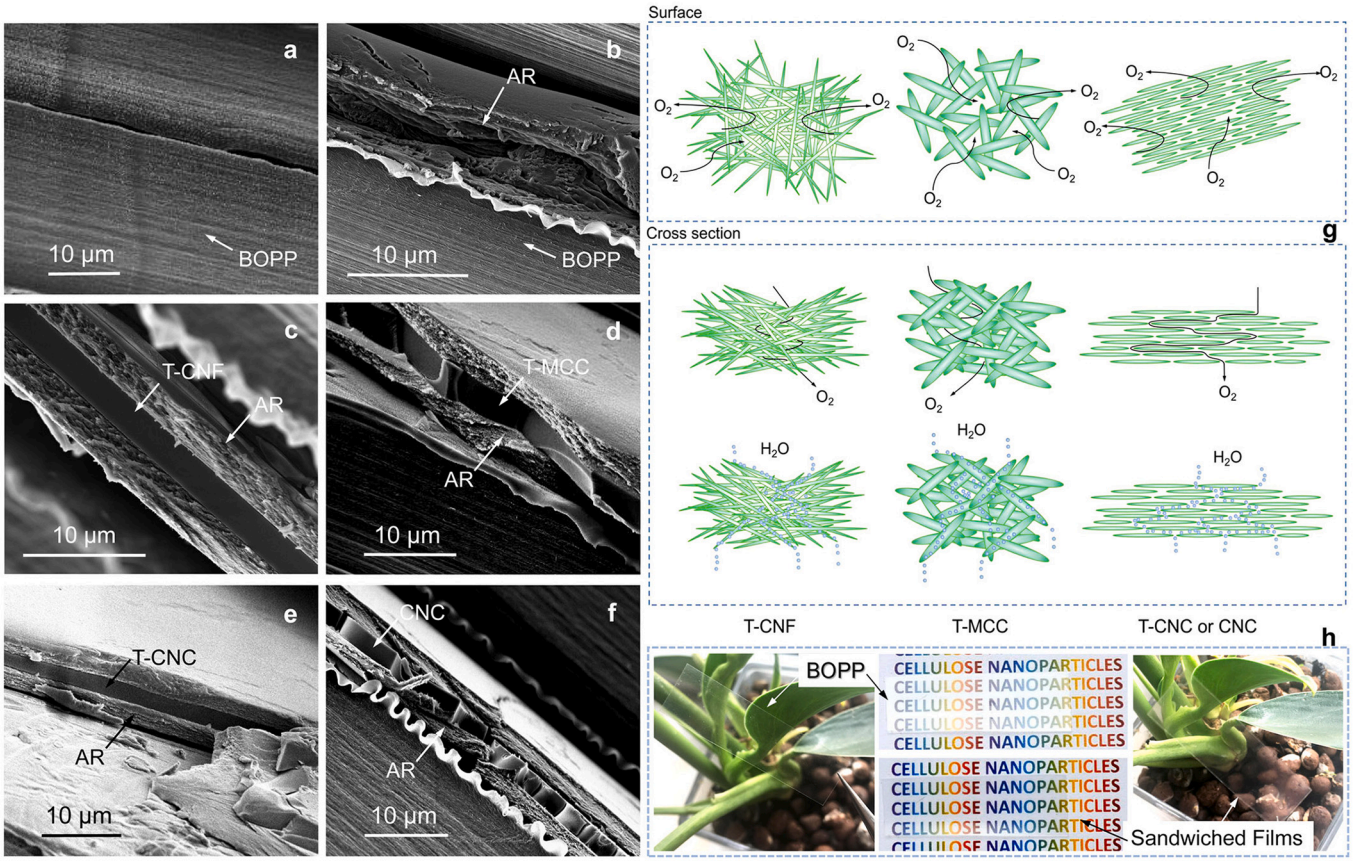

Fig. 3. (a–f) The tearing cross-section morphology of the BOPP and the sandwiched films with different CNP core layers; (g) the O_2 barrier mechanism schematic diagram of CNPs in the plane parallel to the surface of the film (upper) and the O_2 and H_2O moving pathway in cross-section of the CNP layer (lower); (h) digital photograph of the transparent sandwiched films.

Table 3
Thickness, density, and porosity of BOPP, acrylic resin (AR), and CNP layer.

Sample	Thickness(μm)	Density(g/cm^3)	Porosity (%)
BOPP	57 (0.024)	0.91 (0.092)	–
AR	1.58 (0.097)	1.16 (0.020)	–
T-CNF	1.75 (0.029)	1.09 (0.018)	29.7 (1.133)
T-MCC	1.92 (0.123)	1.00 (0.031)	35.5 (1.980)
T-CNC	1.25 (0.113)	1.52 (0.023)	1.9 (1.466)
CNC	1.44 (0.123)	1.33 (0.027)	14.1 (1.736)

thickness reflected the density and porosity of the film. The thinner thickness produced a denser microstructure, forming few and small pores and thus improving the oxygen barrier properties. The results indicate that well-organized CNP layers (T-CNC, CNC layer) show a low porosity, presenting higher oxygen barrier properties.

The chemical groups on the CNP surfaces are another important factor affecting the barrier properties of the film. The hydroxyl and carboxyl groups on the CNC and T-CNP were hydrophilic groups with strong polarity, which led to the high WVTR. Water molecules not only permeated the film via pores, similar to the oxygen molecules but also moved as the primary or secondary absorbed water along the crystal surface (Fig. 3g). The secondary absorbed water molecules showed several layers that increased the distance between crystals, further facilitating water transport. The water vapor pressure and concentration differences across the film promoted the water molecules moving from high water concentration to low water concentration. The water absorption increased the amount of dissolved water in the film, resulting in increased WVTR. Although the T-MCC layer had relatively large micropores, the T-MCCs had large crystal size and high crystallinity. T-CNFs presented large aspect ratios with relatively low crystallinity, and the non-crystalline regions provided more water transport pathways. The T-CNCs and CNCs under the same volume possessed higher surface area. As a result, the sandwiched film with T-MCC had the lowest WVTR.

4. Conclusions

In this work, transparent five-layered cellulose composite films were successfully fabricated by laminating the BOPP, AR, and CNPs with a sandwich structure. The TEMPO-oxidized CNPs with different aspect ratios were prepared. The resultant sandwiched films maintained high light transmittance and relatively high elongation at break, their tensile strengths were enhanced with increased aspect ratios of the CNPs. The CNP layers had various surface roughness and high surface energies due to their film formation structures and hydrophilicity from cellulose. Different aspect ratio of CNPs resulted in network or parallel microstructure or a combination of both. The well-organized CNPs layer had low porosity, tortuous pathway, and thus the lower OTR. The OTR showed a significant dependence on the thicknes, density, and porosity of the CNP layers. However, these hydrophilic CNP layers resulted in higher WVTR as compared with the polymer. The BOPP at the out layer played an isolating role in protecting the CNP layer, leading to a composite film with balanced gas and water vapor barrier properties and mechanical strength.

CRediT authorship contribution statement

Lanxing Du: Writing – original draft, Methodology, Investigation, Formal analysis. **Haonan Yu:** Investigation. **Bohan Zhang:** Investigation. **Ruilin Tang:** Formal analysis. **Yang Zhang:** Methodology,

Validation. **Chusheng Qi:** Validation. **Michael P. Wolcott:** Resources, Supervision. **Zhiming Yu:** Resources, Supervision. **Jinwu Wang:** Conceptualization, Writing – review & editing.

Acknowledgments

This study was financially supported by the Natural Science Fund of Hebei Province (No. C2019204340), Science Research Fund of Hebei Agriculture University (No. YJ201820), and Modern Forestry Group Project of Hebei Agriculture University (XK1008601519). The authors were also grateful to financial support from the Agriculture and Food Research Initiative (AFRI) Competitive grant (No. 2011-68005-30416), USDA National Institute of Food and Agriculture (NIFA) through the Northwest Advanced Renewables Alliance (NARA).

References

Ammala, A., Pas, S., Lawrence, K., Stark, R., Webb, R., & Hill, A. (2008). Poly(m-xylene adipamide)-montmorillonite nanocomposites: Effect of organo-modifier structure on free volume and oxygen barrier properties. *Journal of Materials Chemistry, 18*(8), 911–916.

Aulin, C., & Ström, G. (2013). Multilayered alkyd resin/nanocellulose coatings for use in renewable packaging solutions with a high level of moisture resistance. *Industrial and Engineering Chemistry Research, 52*, 2582–2589.

Chemin, M., Heux, L., Guérin, D., Crowther-Alwyn, L., & Jean, B. (2019). Hybrid gibbsite nanoplatelet/cellulose nanocrystal multilayered coatings for oxygen barrier improvement. *Frontiers in Chemistry, 7*(507), 1–10.

Dou, Y., Pan, T., Xu, S., Yan, H., Han, J., Wei, M., Evans, D., & Duan, X. (2015). Transparent, ultrahigh-gas-barrier films with a brick-mortar-sand structure. *Angewandte Chemie, 127*(33), 9809–9814.

Du, L., Yu, Z., Wang, J., Wolcott, M., Zhang, Y., & Qi, C. (2020). Analyzing the film formation mechanism of cellulose nanoparticles (CNPs) based on the fast freeze-drying morphology. *Cellulose, 27*(12), 6921–6933.

Du, L., Zhong, T., Wolcott, M., Zhang, Y., Qi, C., Zhao, B., Wang, J., & Yu, Z. (2018). Dispersing and stabilizing cellulose nanoparticles in acrylic resin dispersions with unreduced transparency and changed rheological property. *Cellulose, 25*(4), 2435–2450.

Fang, H., Chen, X., Wang, S., Cheng, S., & Ding, Y. (2019). Enhanced mechanical and oxygen barrier performance in biodegradable polyurethanes by incorporating cellulose nanocrystals with interfacial polylactide stereocomplexation. *Cellulose, 26*(18), 9751–9764.

Fotie, G., Gazzotti, S., Ortenzi, M. A., & Piergiovanni, L. (2020). Implementation of high gas barrier laminated films based on cellulose nanocrystals for food flexible packaging. *Applied Sciences, 10*(9), 3201.

Fukuzumi, H., Fujisawa, S., Saito, T., & Isogai, A. (2013). Selective permeation of hydrogen gas using cellulose nanofibril film. *Biomacromolecules, 14*(5), 1705–1709.

Fukuzumi, H., Saito, T., Iwamoto, S., Kumamoto, Y., Ohdaira, T., Suzuki, R., & Isogai, A. (2011). Pore size determination of TEMPO-oxidized cellulose nanofibril films by positron annihilation lifetime spectroscopy. *Biomacromolecules, 12*(11), 4057–4062.

Fukuzumi, H., Saito, T., Iwata, T., Kumamoto, Y., & Isogai, A. (2009). Transparent and high gas barrier films of cellulose nanofibers prepared by tempo-mediated oxidation. *Biomacromolecules, 10*(1), 162–165.

Ghosh, K., Das, K., Ghosh, S., Ganguly, S., Nath, K., & Das, C. (2020). Physico-mechanical, rheological and gas barrier properties of organoclay and inorganic phyllosilicate reinforced thermoplastic films. *Journal of Applied Polymer Science, 49735*.

Jasińska, B., Dawidowicz, A., Goworek, T., & Wawryszczuk, J. (2003). Pore size determination by positron annihilation lifetime spectroscopy. *Optica Applicata, 33*(1), 7–12.

Jung, B., Jung, H., Kang, K., Kim, G., Lee, M., Shim, J., & Hwang, S. (2020). The fabrication of flexible and oxygen barrier cellulose nanofiber/polylactic acid nanocomposites using cosolvent system. *Journal of Applied Polymer Science.* , Article 49536. https://doi.org/10.1002/app.49536

Kim, K., Choi, B., & Jin, J. (2020). Transparent, water-stable, cellulose nanofiber-based packaging film with a low oxygen permeability. *Carbohydrate Polymers, 249*, Article 112863.

Kim, S., Kook, S., O'Rourke, B., Lee, J., Hwang, M., Kobayashi, Y., … Kim, S. (2017). Characterization of pore size distribution (PSD) in cellulose triacetate (CTA) and polyamide (PA) thin active layers by positron annihilation lifetime spectroscopy (PALS) and fractional rejection (FR) method. *Journal of Membrane Science, 527*, 143–151.

Lu, P., Guo, M., Xu, Z., & Wu, M. (2018). Application of nanofibrillated cellulose on BOPP/LDPE film as oxygen barrier and antimicrobial coating based on cold plasma treatment. *Coatings, 8*(6), 207.

Mangaraj, S., Goswami, K., & Panda, K. (2014). Modeling of gas transmission properties of polymeric films used for MA packaging of fruits. *Journal of Food Science and Technology, 52*(9), 5456–5469.

Miao, L., Walton, C., Wang, L., Li, L., & Wang, Y. (2019). Characterization of polylactic acids-polyhydroxybutyrate based packaging film with fennel oil, and its application on oysters. *Food Packaging and Shelf Life, 22*, Article 100388.

Nguyen, H., Hanif, Z., Park, S., Choi, B., Tran, T., Hwang, D., Park, J., Hwang, S., & Oh, D. (2018). Sustainable boron nitride nanosheet-reinforced cellulose nanofiber composite film with oxygen barrier without the cost of color and cytotoxicity. *Polymers, 10*(5), 501.

Nogi, M., & Yano, H. (2008). Transparent nanocomposites based on cellulose produced by bacteria offer potential innovation in the electronics device industry. *Advanced Materials, 20*(10), 1849–1852.

Norrrahim, F., Ariffin, H., Hassan, M. A., Ibrahim, A., & Nishida, H. (2013). Performance evaluation and chemical recyclability of a polyethylene/poly(3-hydroxybutyrate-co-3-hydroxyvalerate) blend for sustainable packaging. *RSC Advances, 3*(46), 24378.

Ogunsona, E., & Mekonnen, T. (2020). Multilayer assemblies of cellulose nanocrystal-polyvinyl alcohol films featuring excellent physical integrity and multi-functional properties. *Journal of Colloid and Interface Science, 580*, 56–67.

Qin, S., Pour, M., Lazar, S., Koklukaya, O., Gerringer, J., Song, Y., Wagberg, L., & Grunlan, J. (2018). Super gas barrier and fire resistance of nanoplatelet/nanofibril multilayer thin films. *Advanced Materials Interfaces, 6*(2), Article 1801424.

Roilo, D., Maestri, C., Scarpa, M., Bettotti, P., & Checchetto, R. (2018). Gas barrier and optical properties of cellulose nanofiber coatings with dispersed TiO_2 nanoparticles. *Surface and Coatings Technology, 343*, 131–137.

Rowe, R. (1978). The measurement of the adhesion of film coatings to tablet surfaces: The effect of tablet porosity, surface roughness and film thickness. *The Journal of Pharmacy and Pharmacology, 30*(6), 343–346.

Saito, T., & Isogai, A. (2006). Introduction of aldehyde groups on surfaces of native cellulose fibers by TEMPO-mediated oxidation. *Colloids and Surfaces A: Physicochemical and Engineering Aspects, 289*(1–3), 219–225.

Siracusa, V., Rocculi, P., Romani, S., & Rosa, M. (2008). Biodegradable polymers for food packaging: A review. trends food sci tech. *Trends in Food Science & Technology, 19*(12), 634–643.

Sonar, R., Al-Ghamdi, S., Marti, F., Tang, J., & Sablani, S. (2020). Performance evaluation of biobased/biodegradable films for in-package thermal pasteurization. *Innovative Food Science & Emerging Technologies, 66*, Article 102485. https://doi.org/10.1016/j.ifset.2020.102485

Sun, X., Wu, Q., Ren, S., & Lei, T. (2015). Comparison of highly transparent all-cellulose nanopaper prepared using sulfuric acid and TEMPO-mediated oxidation methods. *Cellulose, 22*(2), 1123–1133, 2015.

Vartiainen, J., Shen, Y., Kaljunen, T., Malm, T., Vähä-Nissi, M., Putkonen, M., & Harlin, A. (2015). Bio-based multilayer barrier films by extrusion, dispersion coating and atomic layer deposition. *Journal of Applied Polymer Science, 133*(2), 42260.

Vasile, C. (2018). Polymeric nanocomposites and nanocoatings for food packaging: A review. *Materials, 11*(10), 1834.

Wakabayashi, M., Fujisawa, S., Saito, T., & Isogai, A. (2020). Nanocellulose film properties tunable by controlling degree of fibrillation of TEMPO-oxidized cellulose. *Frontiers in Chemistry, 2020*(8), 1–9.

Wang, C., Shi, J., He, M., Ding, L., Li, S., Wang, Z., & Wei, J. (2018). High strength cellulose/ATT composite films with good oxygen barrier property for sustainable packaging applications. *Cellulose, 25*(7), 4145–4154.

Wang, J., Gardner, D. J., Stark, N. M., Bousfield, D. W., Tajvidi, M., & Cai, Z. (2017). Moisture and oxygen barrier properties of cellulose nanomaterial-based films. *ACS Sustainable Chemistry & Engineering, 6*(1), 49–70.

Wang, L., Chen, C., Wang, J., Gardner, D. J., & Tajvidi, M. (2020). Cellulose nanofibrils versus cellulose nanocrystals: Comparison of performance in flexible multilayer films for packaging applications. *Food Packaging and Shelf Life, 23*, Article 100464.

Wu, C., Saito, T., Fujisawa, S., Fukuzumi, H., & Isogai, A. (2012). Ultrastrong and high gas-barrier nanocellulose/clay-layered bomposites. *Biomacromolecules, 13*(6), 1927–1932.